A&A 486, 577–587 (2008)
DOI: 10.1051/0004-6361:20079231

Astronomy & Astrophysics

Fast events and waves in an active region of the Sun observed in Hα with high spatial resolution

B. Sánchez-Andrade Nuño[1,2], N. Bello González[2], J. Blanco Rodríguez[2], F. Kneer[2], and K. G. Puschmann[2,3]

[1] Max-Planck-Institut für Sonnensystemforschung, Max-Planck-Str. 2, 37191 Katlenburg-Lindau, Germany
[2] Institut für Astrophysik, Friedrich-Hund-Platz 1, 37077 Göttingen, Germany
e-mail: [bruno;nazaret;blanco;kneer]@astro.physik.uni-goettingen.de
[3] Instituto de Astrofísica de Canarias, C/ vía Láctea, s/n, 38205 La Laguna, Tenerife, Spain
e-mail: kgp@iac.es

Received 11 December 2007 / Accepted 28 April 2008

ABSTRACT

Context. We study the chromosphere of an active region of the Sun in the Hα line.
Aims. The development of new instrumentation and new methods of data analysis allows to scrutinize the dynamics of the solar chromosphere with high spatial, spectral, and temporal resolution. The observations we present shed light on some magneto-dynamic processes occurring above an active region in the chromosphere.
Methods. We took a time series of 55 min in Hα from AR 10875 at $\vartheta \approx 36°$. We used the "Göttingen" Fabry-Perot spectrometer at the Vacuum Tower Telescope, Observatorio del Teide/Tenerife, to obtain two-dimensional spectrograms in Hα. Adaptive optics and image reconstruction yielded a spatial resolution better than 0.″5 throughout the time sequence. From the wealth of structures, we selected areas of interest to study further, in detail, some ongoing processes.
Results. A small straight surge developed aside of a pore with upward phase speed of 100 km s^{-1} and line-of-sight (LOS) velocity of 15 km s^{-1}. The surge retreated rapidly with LOS velocity of 45 km s^{-1} at its mouth. It underwent a rebound and fell back again. Two sympathetic mini-flares were observed that lasted only approximately 40 s, but showed strong Hα emission. We found magnetoacoustic waves in long fibrils as mainly short wave trains, short packets or pulses, i.e., solitary waves consisting of small (1″–2″) blobs. They start at either end of the fibrils and travel with phase speeds of 12–14 km s^{-1}, i.e., close to the tube speed and approximately the sound velocity for sufficiently large magnetic field strengths. Some waves speed up to reach velocities of the order of 30 km s^{-1}. This is much lower than the expected Alfvén velocity of ≥200 km s^{-1} for reasonable magnetic field strengths and mass densities. We suggest that slow waves are not purely longitudinal, but possess gas velocities perpendicular to the direction of propagation of few km s^{-1}. Also, fast waves travel along sinuous lines suggesting entangled magnetic fields. They spread out along the direction of propagation in the course of their evolution and often vanish. We discuss the implications.

Key words. Sun: chromosphere – Sun: activity – Sun: oscillations – techniques: high angular resolution – techniques: spectroscopic

1. Introduction

Since its discovery 150 years ago, the chromosphere of the Sun has remained a lively and exciting field of research. The chromosphere of active regions especially exhibit a wealth of dynamic interaction of the solar plasma with magnetic fields. The literature on the solar chromosphere, and on stellar chromospheres, is numerous. We thus restrict citations to the monographs by Bray & Loughhead (1974) and Athay (1976) and to the more recent proceedings from the conferences *Chromospheric and Coronal Magnetic Fields* (Innes et al. 2005) and *The Physics of Chromospheric Plasmas* (Heinzel et al. 2007).

Our study concentrates on fast phenomena and waves observed in the Hα line in an active region with high spatial, temporal and wavelength resolution. Ejecta from low layers of active regions, called surges, have been observed in time sequences of Hα filtergrams for many decades (e.g., Tandberg-Hanssen 1977). Fast downflows from the corona, observed in the XUV and in Hα were recently discussed by Tripathi et al. (2007, and references therein). Fast horizontal, apparent displacements of small bright blobs with velocities of up to 240 km s^{-1} were observed in Hα by van Noort & Rouppe van der Voort (2006). We have reported previously on obliquely downward moving Hα structures with velocities of 100 km s^{-1} (Sánchez-Andrade Nuño et al. 2005a,b).

Apart from oscillations in sunspot umbrae (Beckers & Tallant 1969; Wittmann 1969) and running penumbral waves (e.g., von Uexküll et al. 1983, and references therein), waves in the chromosphere were observed by many authors. Giovanelli (1975), e.g., describes waves along Hα mottles and fibrils with speeds of 70 km s^{-1} and interprets them as Alfvén waves in magnetic flux tubes with approximately 10 Gauss field strength. Kukhianidze et al. (2006), from time sequences in Hα off the limb, found kink waves in spicules with periods of 35–70 s. Hansteen et al. (2006) and Rouppe van der Voort et al. (2007) observed spicules and fibrils in the quiet Sun and in active regions with high spatial and temporal resolution observations. They succeeded via numerical simulations in explaining the dynamics of these chromospheric small-scale structures by magnetoacoustic shocks, excited mainly by the solar 5-min oscillations (see also the simulations by Sterling & Hollweg 1989; and the review by Carlsson & Hansteen 2005).

Waves in the corona have been observed as well: e.g., Robbrecht et al. (2001) report on slow magnetoacoustic waves in coronal loops observed in high-cadence images from SoHO/EIT (Solar & Heliospheric Observatory/Extreme

ultraviolet Imaging Telescope) and TRACE (Transition Region and Coronal Explorer). The speeds amount to 100 km s^{-1}. De Moortel et al. (2002), also from high-cadence 171 Å TRACE images, find that 3- and 5-min oscillations are common in coronal loops. They are also interpreted as magnetoacoustic waves. Tothova et al. (2007), from SoHO/SUMER (Solar Ultraviolet Measurements of Emitted Radiation) data, study Doppler shift oscillations identified as slow mode standing waves in hot coronal loops. Fast-mode, transverse, incompressible Alfvén waves, with speeds of 2 Mm s^{-1}, in the solar corona were reported by Tomczyk et al. (2007).

For theoretical treatments of waves in magnetized plasmas we refer to the textbooks by Ferraro & Plumpton (1966) and Priest (1984). The propagation of waves in magnetic flux tubes were treated by, among others, Defouw (1976), Wentzel (1979), Spruit (1982), and recently by Musielak et al. (2007).

The present work deals with dynamic phenomena in the active solar chromosphere. We describe in Sect. 2 the observations obtained in the Hα line with a two-dimensional Fabry-Perot spectrometer and the basic data reduction with speckle methods, yielding very high spatial resolution. Section 3 contains two specific analyses and results in fast events observed in a very active region, and Sect. 4 contains further analyses to highlight the observations of fast and slow mode waves in systems of elongated fibrils in the same active region. Such long fibrils are the best candidates to study magnetoacoustic waves, which are expected to arise from buffeting of magnetic fields at the fibrils' rooting in the photosphere. We also discuss the results on magnetoacoustic waves. Section 5 concludes the paper.

2. Observations and data reduction

2.1. Observations

On April 26, 2006, we observed the active region AR 10875 in Hα with the Vacuum Tower Telescope at the Observatorio del Teide/Tenerife. The large, flaring region was located at heliographic coordinates of approximately E36°, S10°, and at heliocentric angle $\vartheta \approx 36°$. The observations were supported by the Kiepenheuer Adaptive Optics system (KAOS, von der Lühe et al. 2003). We obtained a time sequence of 55 min with a mean cadence of 22 s between 7:52:30 and 8:47:42 UT. We used the two-dimensional "Göttingen" spectrometer (Bendlin & Volkmer 1995; Volkmer et al. 1995; Koschinsky et al. 2001) with the upgrades described by Puschmann et al. (2006). At each of 21 wavelength positions around Hα line center, 15 narrow-band images (*FWHM* ≈ 45 mÅ) were taken. The wavelength interval amounted to 100 mÅ, the exposure time was 5 ms. We recorded broadband images at 6300 Å through a filter with approximately 50 Å *FWHM* simultaneously with the narrow-band frames. For standard data analysis, dark frames were taken along with flat field exposures with moving pointing around the disc center.

Due to a technical problem, we notice an increasing delay between successive scans during the observations. When the accumulative delay reached around seven seconds a new scanning procedure was restarted to avoid higher gaps between frames. This operation takes around one minute. During the 55 min of the series, such an interruption occurred twice, at 08:10:19 UT and 08:29:46 UT. The programming bug was corrected afterward for future observations.

2.2. Data analysis

We subjected all data to dark subtraction and flat fielding. For each scan, a reconstructed broadband image was obtained with the speckle code developed in Göttingen (de Boer 1996). It uses the spectral ratio method to correct the amplitudes (von der Lühe 1984) and speckle masking (Weigelt 1977) to retrieve the phases. This version takes into account the field dependence of the AO correction (Puschmann & Sailer 2006). We achieve a spatial resolution of ~0.″25 for these broadband images at 630 nm.

With the good estimates of the broadband objects, the narrow-band images were reconstructed following the standard method (see, e.g., Keller & von der Lühe 1992; Krieg et al. 1999; Bello González et al. 2005): We denote, in Fourier space, the $i = 1 \ldots N$ narrow-band exposures at one wavelength position by $I_{\mathrm{n},i}$; the simultaneously taken broadband frames by $I_{\mathrm{b},i}$; and the estimate of the broadband scenery by O_{b}. The reconstructed narrow-band image at a specific wavelength is then obtained from

$$O_{\mathrm{n}} = H \frac{\sum_{i=1}^{N} I_{\mathrm{n},i} I_{\mathrm{b},i}^{*}}{\sum_{i=1}^{N} |I_{\mathrm{b},i}|^{2}} O_{\mathrm{b}}. \quad (1)$$

Here, "*" indicates the conjugate complex, and H is a (real) filter. The spatial resolution of the reconstructed frames is better than 0.″5.

To follow the temporal evolution in time, both broadband and narrow-band images were cropped to the same common FOV (Field of View), removing overall image shifts due to residual seeing effects. Afterward, the speckle reconstructed broadband images were co-aligned to spatially and temporally smoothed images via a destretching code provided by Yi & Molowny Horas (1992). We also applied the destretching matrix from the broadband image to the simultaneous narrow-band scan. To minimize the effects of the irregular sampling rate, the time sequences were interpolated to equidistant times with the cadence that leads to a minimum shift in time for each frame. This corresponds to a regular time step of 22 s. The data gaps at the times when interrupted observation were filled by linear interpolation between closest observed images.

Figures 1 and 2 give respectively the broadband scenery at $t = 15.4$ min during the series and the associated Hα image at +0.5 Å off line center. The whole region was very active with a flare occurring during the observation of the time sequence (Sánchez-Andrade Nuño et al. 2007). The data set is certainly rich with information on the dynamics of the active chromosphere, especially since the spatial resolution is high throughout the sequence. For the present study, we restrict further analyses and discussions to few regions. The areas of interest (AOIs) are indicated by rectangles and denoted by A, B, B′, C, and D. In the presentations below, we rotated the images from the AOIs to have their long sides parallel to the spatial co-ordinate in space-time images. AOI A contains a region where a long fibril developed twice during our observations. It has the appearance of a small surge (Tandberg-Hanssen 1977). The AOIs B and B′ show a simultaneous fast event, possibly "sympathetic" mini-flares with strong, small-scale brightenings in the Hα line core that last only few tens of seconds. The AOIs C and D, with their long fibrils, are suitable for the study of magnetoacoustic waves along magnetic field lines. Area C contains, in its right part, a region from which Hα fibrils stretch out to both sides and which, at the beginning of the time sequence, contained a small pore that disappeared in the course of the observations. Note also, from Fig. 1, that the fibrils on the upper left side of area D originate in the penumbra of a small sunspot.

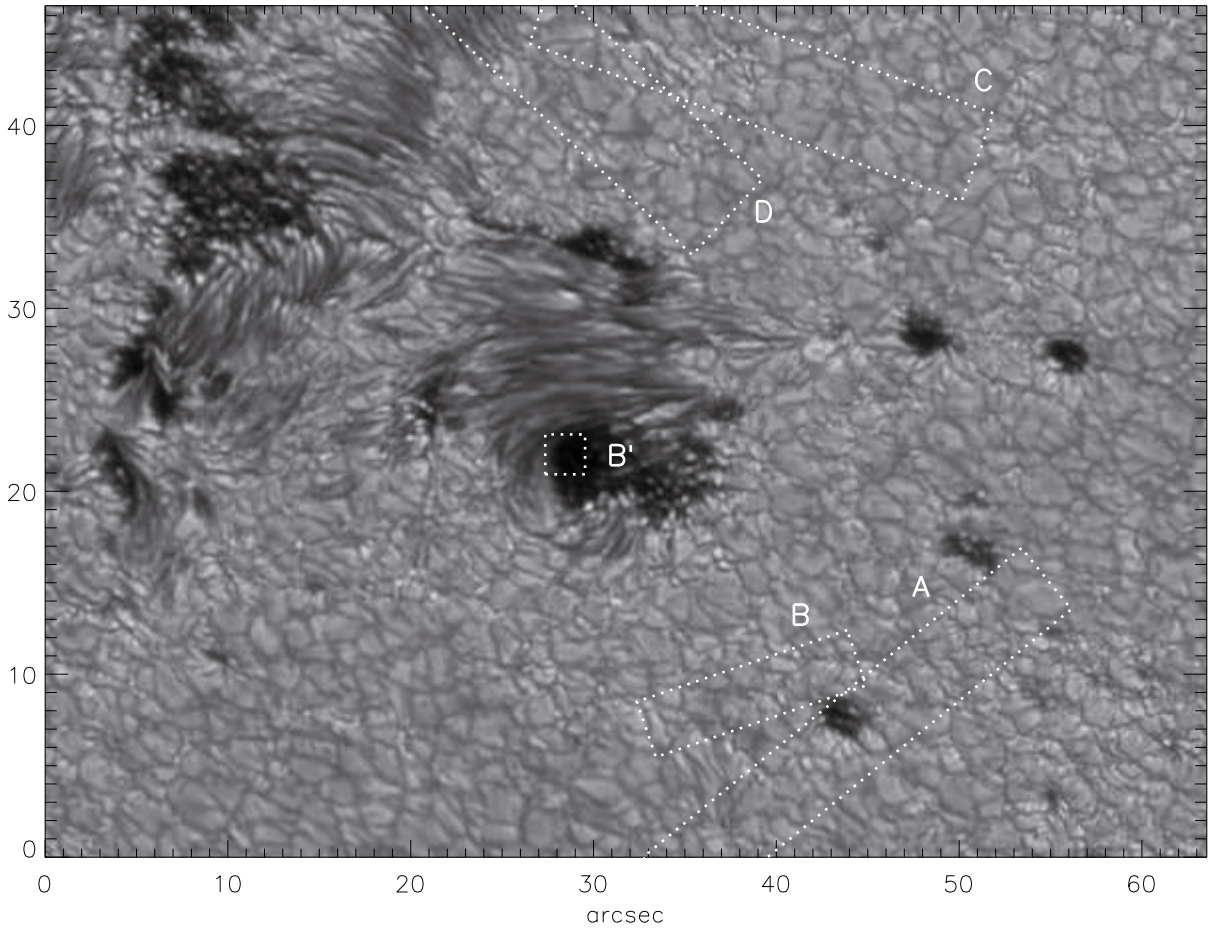

Fig. 1. Broadband image of part of the active region AR10875 observed on April 26, 2006 at heliocentric angle $\vartheta = 36°$. The image is from time $t = 15.4$ min after the start of the series. The rectangles, denoted by A, B, B′, C, and D, are the areas of interest (AOIs) to be analyzed and discussed in the present work.

2.3. Physical parameters

The possibility of extracting information from a good part of the Hα line profile in two dimensions and along the time series is highly valuable. One can interpret emission in the line core as a result of injection of high 'temperature' electrons into the chromosphere (e.g., Al et al. 2004). Furthermore, we are interested in the physical parameters of the Hα structures; their line-of-sight velocities $v_{\rm LOS}$; their temperatures; and their mass densities to be retrieved from the line profiles. Under the assumption that the structures are isolated and at large heights above the unperturbed chromosphere, the parameters can be retrieved from Beckers's (1964) "cloud model". When calculating the intensity $I(\lambda)$ emerging from a cloud with source function S irradiated from below by the reference intensity $I_0(\lambda)$, the contrast profile $C(\lambda)$ is given by

$$C(\lambda) = \frac{I(\lambda) - I_0(\lambda)}{I_0(\lambda)} = \left(\frac{S}{I_0(\lambda)} - 1\right) \cdot (1 - \mathrm{e}^{-\tau(\lambda)}), \qquad (2)$$

where

$$\tau(\lambda) = \tau_0 \cdot \exp\left[-\left(\frac{\lambda - \lambda_{\rm c}(1 - v_{\rm LOS}/c)}{\Delta\lambda_{\rm D}}\right)^2\right] \qquad (3)$$

describes the wavelength dependence of the optical thickness τ by a Gaussian. Here, τ_0 stands for the optical depth at the line center, $\lambda_{\rm c}$ for the wavelength of the line center, $\lambda_{\rm c}(v_{\rm LOS}/c)$ for the shift due to the macroscopic LOS velocity, and $\Delta\lambda_{\rm D}$ for the Doppler width. (Our convention is that velocities are positive toward the observer.)

The cloud model inversion, i.e., fitting the contrast profiles from Eq. (2) with the parameters S, τ_0, $\lambda_{\rm c}(v_{\rm LOS}/c)$, and $\Delta\lambda_{\rm D}$ to the observed contrasts, has been used extensively, e.g., by Tsiropoula & Schmieder (1997); Al et al. (2004); Tsiropoula & Tziotziou (2004); Tziotziou et al. (2004), see also the recent review by Tziotziou (2007). A more refined method was employed by Tsiropoula (2000).

Here, we also used the inversion in Hα structures where possible. The region under study was "clouded out" in Hα, i.e., covered with structures to a large extent, and the cloud model inversion failed often. In these latter cases, instead, we determined the LOS velocity maps from difference images at Hα ± 0.5 Å off line center with appropriate scaling, i.e., transforming intensity differences to velocities by means of the line slopes. Calibration curves to estimate from such Doppler-grams the true velocities were calculated by Georgakilas et al. (1990). For this, we calculated from the Doppler-grams what these authors denote as Doppler signals. Adopting for the Hα structures reasonable line center optical depths of $\tau_0 \approx 1$, and Doppler widths of $\Delta\lambda_{\rm D} \approx 0.4$ Å (see, e.g., Tsiropoula & Schmieder 1997; Tsiropoula 2000; Tsiropoula & Tziotziou 2004), we found that the velocities from the difference images were lower by a factor 2–4 than the true velocities in agreement with those parts in the FOV where the cloud model inversion was successfully applied and with the

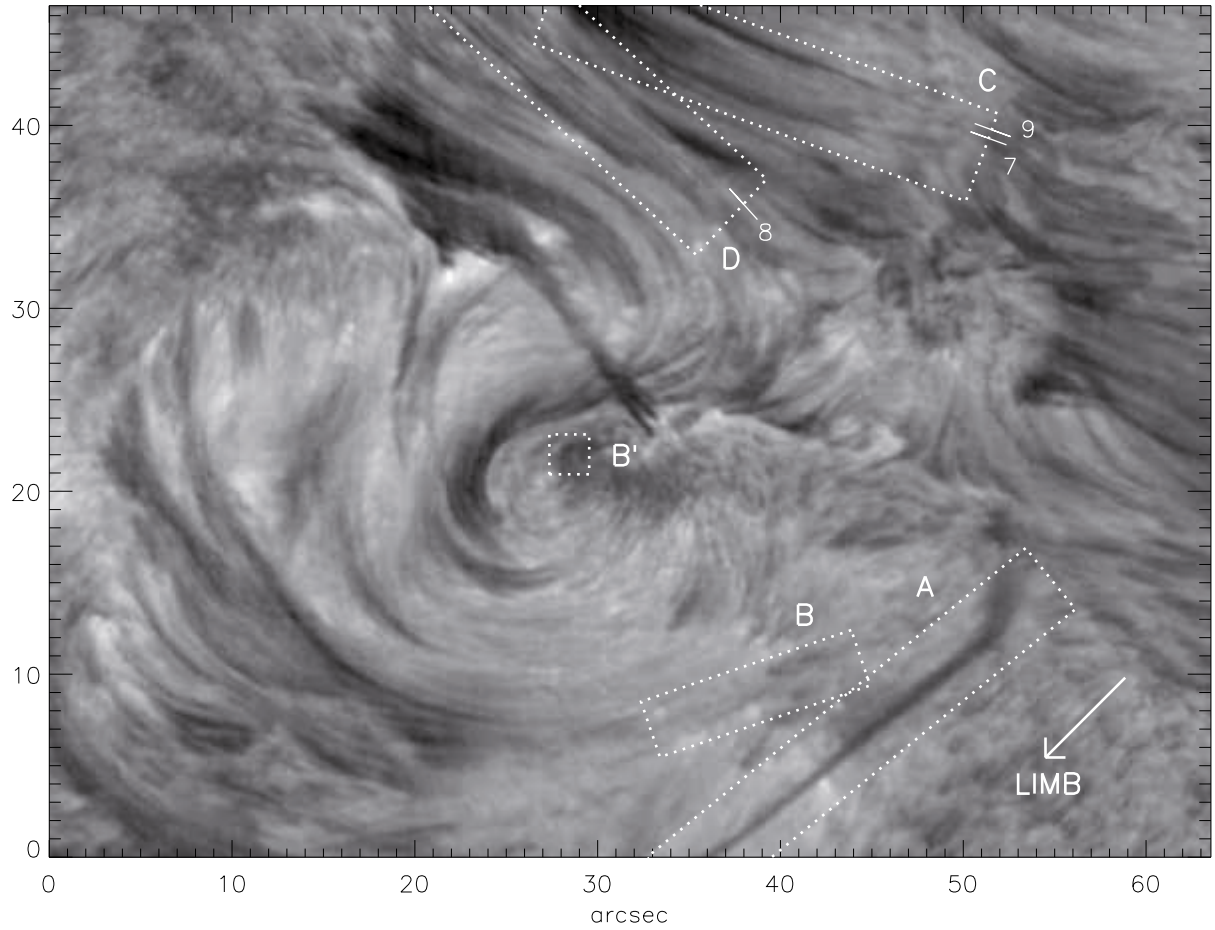

Fig. 2. Narrow-band image corresponding to Fig. 1 in Hα at +0.5 Å off line center. The same areas of interest are indicated as in Fig. 1 by the rectangles. The short lines with the numbers 7−9 indicate locations of the space-time slices that are the subjects of Figs. 7 to 9. The surge in AOI A occurred at a later time. So this figure is a montage with the surge mounted on it from time t = 40.9 min during the series.

results by Tziotziou et al. (2004). Derivations of other parameters, such as (electron) temperature T_e, mass density ρ, gas pressure p, hydrogen density N_H, and electron densities N_e, were given for a wide range of chromospheric structures by Tsiropoula & Schmieder (1997); Tsiropoula (2000); Tsiropoula & Tziotziou (2004); Bostancı (2005).

Table 1 summarizes the results from the cloud model and derived quantities for the surge in Fig. 2, AOI A, and Fig. 3. As reference profile $I_0(\lambda)$, we took an average quiet Sun profile, close, but outside the FOV of Fig. 3. The first two rows result from the inversion technique while we derived the other parameters from them. We assumed a LOS thickness equal to the width of the fibril (cylindrical shape) of 590 km and a micro-turbulent velocity of 10 km s^{-1}. The particle densities in the hydrogen levels 1−3 are denoted as N_1, N_2, and N_3, respectively. The column mass density across the structure M; c_s the sound velocity in the structure; and $x_H \approx N_e/N_H$ the ionization degree of hydrogen.

Table 1. Several derived parameters from the cloud model for the lower-half section of the surge in Figs. 2 (AOI A) and 3 at t = 39.7 min.

Parameter	Av. value	Parameter	Av. value
v [km s^{-1}]	11.7	$\Delta\lambda_D$ [Å]	0.34
S/I_c	0.154	τ	1.05
N_2 [cm^{-3}]	4.5×10^4	N_e [cm^{-3}]	6.8×10^{10}
N_H [cm^{-3}]	1.1×10^{11}	N_1 [cm^{-3}]	3.8×10^{10}
N_3 [cm^{-3}]	4.2×10^2	T_e [K]	1.51×10^4
p [dyn cm^{-2}]	0.38	M [g cm^{-2}]	1.39×10^{-4}
ρ [g cm^{-3}]	2.3×10^{-13}	x_H	0.64
c_s [km s^{-1}]	14.4		

3. Fast events in Hα

Small recurrent surge

In AOI A, a surge occurred during the observed time series. It started near the pore at the upper right end of region A (cf. Figs. 1 and 2). It was straight and thin, with a projected length at its maximum extension of at least 15 Mm and with widths of approximately 1″ near its mouth and 0.″6 at its end. Figure 3 shows the temporal evolution of the surge in Hα +0.5 Å off line center. The space-time image starts 14.7 min after the beginning of the series and goes to the end of it. Along the spatial axis and at each temporal position in Fig. 3, the minimum intensities across the surge at +0.5 Å off line center are shown.

The surge consisted of very thin fibrils, at the resolution limit <0.″5, being ejected in parallel, and then becoming darker, or more numerous, i.e., more opaque. It started with several small elongated clouds lasting for 1−2 min. Afterward, it rose, reaching a projected length of around 14 Mm, and fell back after ∼7 min. Then, it suddenly rose again after 2 min, reaching lengths out of the FOV (more than 15 400 km) and lasted another five min before retreating again. And finally, the

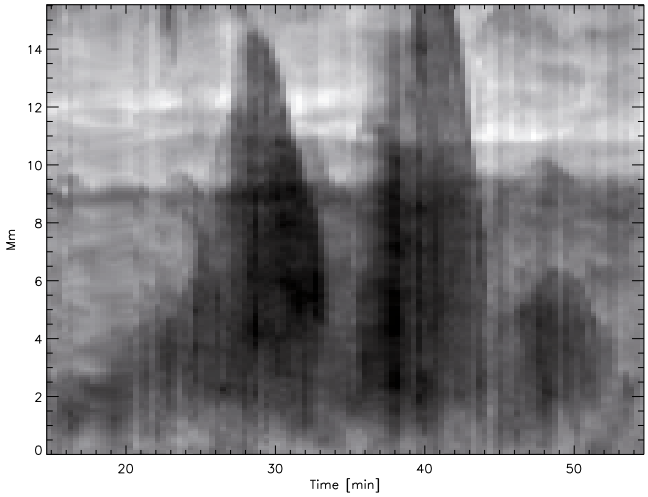

Fig. 3. Space-time image of surge in AOI A at Hα +0.5 Å off line center, starting at 14.7 min after the beginning of the sequence. Along the spatial axis and at each time step, the minimum intensities across the surge at this wavelength are given.

process recurred a third time, yet with lower amplitude in extension and velocity than the first two times. The (projected) proper motion of the tip of the surge reaches a maximum velocity of approximately 100 km s^{-1} for both the ascent and the descent phases. The second rise and fall showed specially large velocities. It is unlikely that the rapid rise and appearance of the surge in Hα are caused by cooling of coronal gas to chromospheric temperatures. The cooling times are much too long, of the order of hours (Hildner 1974). Thus, the proper motions represent gas motions. The LOS velocities measured from Dopplergrams and corrected with the calibrations described above in Sect. 2.3, amounted to +15 km s^{-1} during the ascent of the surge and reached −45 km s^{-1} at the mouth during retreat. These latter velocities are lower than the proper motions. It thus appears that the chromospheric gas is ejected obliquely into the direction toward the limb. Average physical parameters in the surge obtained with the cloud model inversion are listed in Table 1. They are very similar to those of other chromospheric structures (see, e.g., Tsiropoula & Schmieder 1997).

Surges are known to show a strong tendency to recur, but on timescales of ∼1 h. Sterling & Hollweg (1989) have treated numerically rebound shocks in chromospheric fibrils and presented results in which a single impulse at the base of the involved magnetic flux tube drives a series of shocks on timescales of approximately 5 min. This appears to be a viable mechanism for the small surge observed here, apart from the initial conditions. The small "firings" at the beginning of this surge suggest magnetic field dynamics that ultimately cause a strong impulsive force, after some minor events.

Synchronous flashes

In the AOI pair (B, B′) with a projected distance of 13.7 Mm, brightenings occurred at $t = 52.2$ min after the start of the series and in both sites simultaneously within the measurement uncertainties. The AOI B′ is located in the umbra of a small spot with a complex penumbra and AOI B is located next to a pore. In between the two AOIs, the sigmoidal filament ended while more structures of the extended and active filament system crossed the region between the two AOIs. Figure 4 shows the temporal evolution of the brightenings. It is important to note that for the interpretation and discussion of these short-lived synchronous flashes, we used the original data *without interpolation of the images to an identical time*. The upper row of this figure is from AOI B′, the lower from B. Two scans through the Hα profile are presented. The horizontal axes contain the run in both time and wavelength.

The flash-like brightenings only lasted for less than 45 s; they were not present in the scans before or after the two scans shown in Fig. 4. The simultaneity of the two flashes, or mini-flares, suggests a relation between them. We are possibly seeing sympathetic flares. These were discussed earlier in the context of synchronous flares excited by activated filaments (Tandberg-Hanssen 1967). Another interpretation is that we are seeing a mini-version of two-ribbon flares with a common excitation in the corona above them and a simultaneous injection of electrons into the chromosphere.

In AOI B, the flash exhibited sub-structure and apparently moved during the first presented scan with speeds up to 200 km s^{-1}. This strong brightening between 15 and 22 s disappeared in the following scan.

Figure 5 depicts the recorded Hα profiles at the positions of the flash in AOI B, as indicated by the arrows on the left side of Fig. 4. The profiles are compared with those from the quiet Sun and from the average background. The profile from the isolated bright blob at 3.7 Mm (see inset in Fig. 5) shows a blue shifted emission above the background profile. This emission is still present in the following scan. At 2.8 Mm, the line core is filled resulting in a contrast profile with strong emission (cf. Eq. (2)). The profile at 1.1 Mm exhibits a strong emission beyond the continuum intensity in the red wing, while the whole profile is enhanced above the background profile. The position of the emission peak would indicate a downflow with LOS velocity of 35 km s^{-1}. Al et al. (2004) showed that such emission (contrast) profiles can be understood if one assumes an injection, likely from the corona, of much energy and electrons to obtain a response of the Hα line to temperature. These last two emissions at 2.8 Mm and 1.1 Mm disappeared at the time of the following scan.

Obviously, such fast events as in AOIs B and B′ lie beyond the observing capabilities of our consecutive scanning method. We could, however, retrieve high-spatial resolution filtergrams at several wavelengths to follow the temporal evolution at timescales of a few seconds. With the present data set, we cannot decide whether the apparent proper motion of the flashing structure in AOI B is indeed as high as 200 km s^{-1}, or whether the temporal resolution is too fast for the consecutive scanning. For example, the Hα profile from 1.1 Mm could have been in emission over the whole profile, but only for a few seconds. It is, however, possible to design adequate observing sequences of a few seconds per scan at the expense of taking filtergrams at fewer wavelength positions.

4. Magnetoacoustic waves in long Hα fibrils

4.1. Observational results

The intensities and LOS velocities of the structures contain variations on long timescales of 10 min and longer as well as fluctuations with shorter timescales. To distill the latter, among them possible fluctuations due to magnetoacoustic waves, we applied a high-pass temporal filter to the measured intensities and velocities; and removed some high-frequency noise at the same time. The quantities then fluctuate around zero. Figure 6 depicts the average power spectra of the LOS velocities from the whole

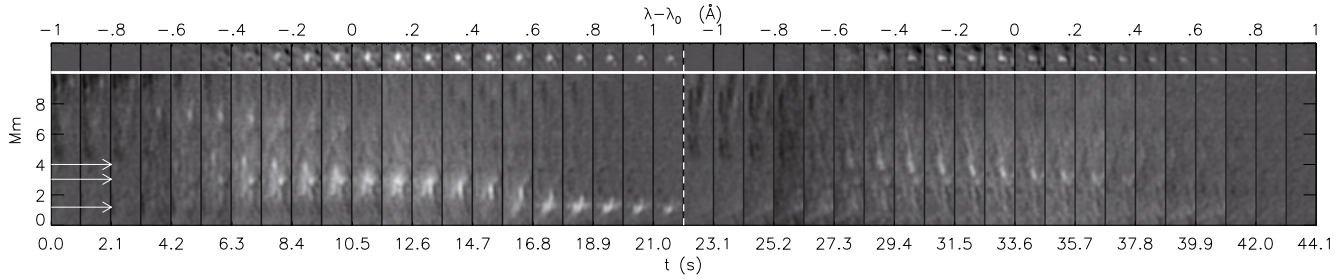

Fig. 4. Simultaneous flash event on AOI B and B′ with projected distance of 13.7 Mm. A pair of simultaneous, short brightenings was recorded at t = 52.2 min. *Top row* from B′, *bottom row* from B. The tiles *from left to right* correspond to two successive Hα scans. *Upper* x-axis is scaled to the wavelength of each 2D filtergram tile. Scanning time is numbered on *the lower* x-axis where $t = 0$ corresponds to the beginning of the scan at 08:44 UT. The integration time for each spectral position is ≈1 s, while the delay between two scans is ≈3 s (vertical dashed line). Each spectrogram on B is normalized with the background profile (see Fig. 5) to emphasize the flash event. Neither the previous nor the following scan of the two presented exhibited any emission. The second scan (right half size of the figure) still shows some emission on the same position. White arrows correspond to the position of the three different profiles shown in Fig. 5.

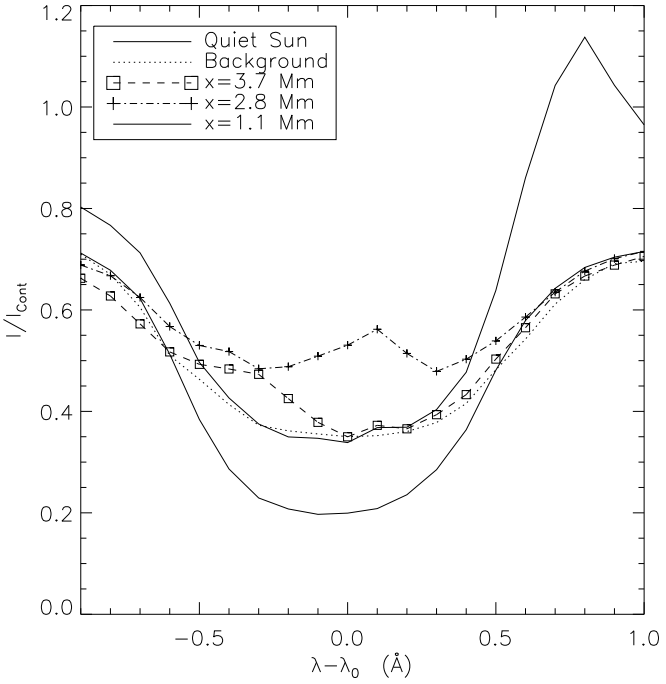

Fig. 5. Hα profiles from the flash event. Each profile corresponds to an average over three pixels around the three selected points where the emission is highest in the blue wing, at central wavelength, and in the red wing, corresponding to the white arrows in Fig. 4 (left half) at x = [3.7, 2.8, 1.1] Mm, respectively. For comparison the quiet Sun profile, from a nearby quiet area outside the FOV, is also shown. Background profile corresponds to the mean from previous and following scans, where no brightening was found. The emission profile at 1.1 Mm reaches an intensity >1.1 of the quiet Sun continuum intensity.

AOI C before and after filtering. The velocities are those measured in Doppler-grams. We note that the 5-min oscillations are filtered out, while some oscillations at the acoustic cutoff (corresponding to periods of approximately 200 s) are partially retained. Yet the unfiltered and filtered power spectra in Fig. 6 do not show any predominant period.

Figures 7–9 show examples of space-time slices from AOIs C and D. The *fluctuations* of several quantities are shown:

1. LOS velocities determined from differences of Hα intensities at ±0.5 Å off line center, henceforth referred to as Doppler-gram slices (bright indicates velocity towards observer);
2. Hα line center intensities, henceforth LC slices;

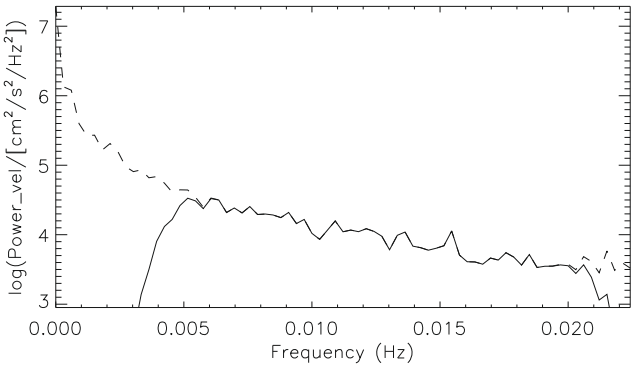

Fig. 6. Average temporal power spectra of velocity from AOI C in Figs. 1 and 2 before filtering (dashed) and after pass-band filtering (solid).

3. in Figs. 7 and 8 differences of intensities at +0.5 Å off line center $I_{0.5}(t_{i+1}) - I_{0.5}(t_i)$ with cadence $\Delta t = t_{i+1} - t_i$ = 22 s, henceforth referred to as $\Delta I_{0.5}$ slices; and
4. in Fig. 9, differences of intensities at line center $I_{\rm LC}(t_{i+1}) - I_{\rm LC}(t_i)$, henceforth referred to as $\Delta I_{\rm LC}$ slices.

Time runs from bottom to top with $t = 0$ at the start of the series. The interruptions/interpolations at $t \approx 18.0-19.6$ min and 37.5−38.5 min are obvious.

The oblique stripes in Figs. 7–9 are the signatures of magnetoacoustic waves. From their slopes we can measure phase velocities projected on the plane perpendicular to the LOS. In Fig. 7 from AOI C, the waves appear to originate near the right edge of the AOI. This is one side at which the fibrils are rooted. Presumably, the waves are excited by the buffeting of motions at the photospheric foot points of the magnetic fields. As seen especially well in the Doppler-gram slices of Fig. 7, but also in the LC slices, steep stripes originate and propagate to opposite directions from this region where the fibrils are rooted. The projected phase speeds are of the order of 8 km s^{-1}. Oblique stripes also originate at the left end of the stripes and propagate toward the center. This is seen in the Doppler-gram and LC slices starting at $t \approx 40$ min. Space-time slices from other positions in AOI C exhibit the origin of waves on the left side in a more pronounced manner, but are not represented here.

Once detected, the signatures of magnetoacoustic waves can be seen in all space-time slices, along the whole time series. During some periods, they are best observable in LC, as in the time interval 0−15 min in Fig. 7, and at other periods they are

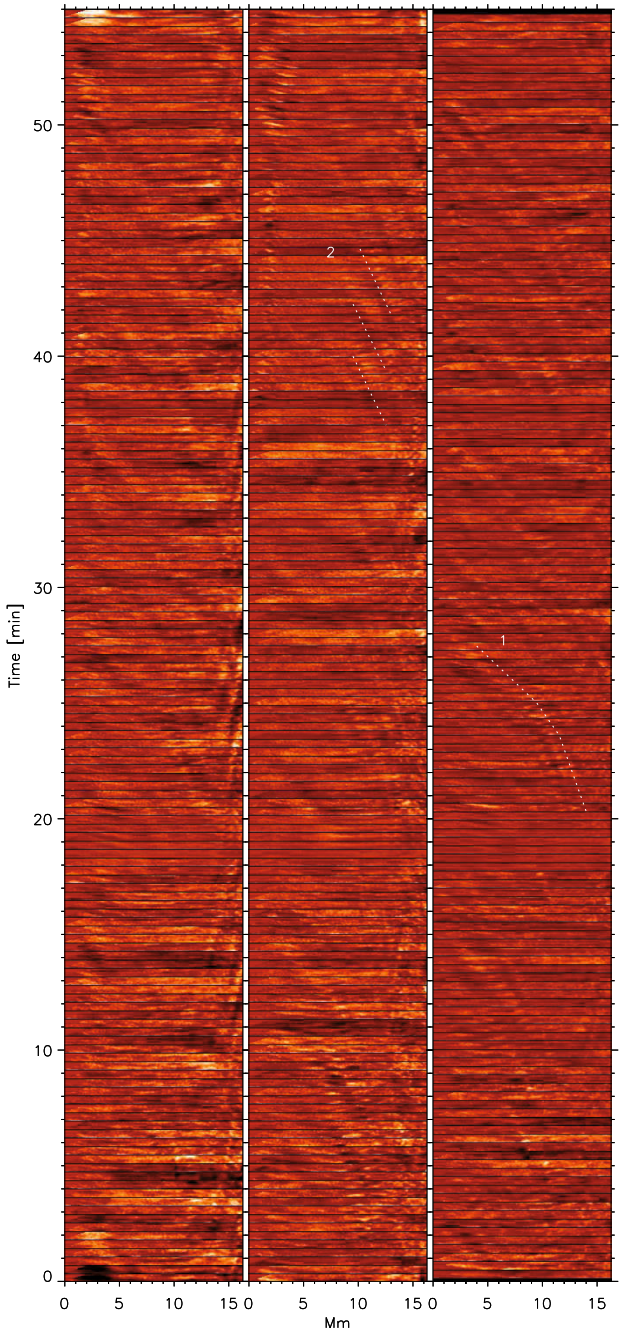

Fig. 7. Example of space-time slices, of 1.″1 width, from AOI C in Figs. 1 and 2. *From left to right*: LOS velocity, Hα line center intensity, and intensity differences at Hα +0.5 Å off line center: $I_{0.5}(t_{i+1}) - I_{0.5}(t_i)$ with cadence of $\Delta t = t_{i+1} - t_i = 22$ s. The intensity differences in the right column are shifted up by 11 s. They are referred to as $\Delta I_{0.5}$ slices in the text.

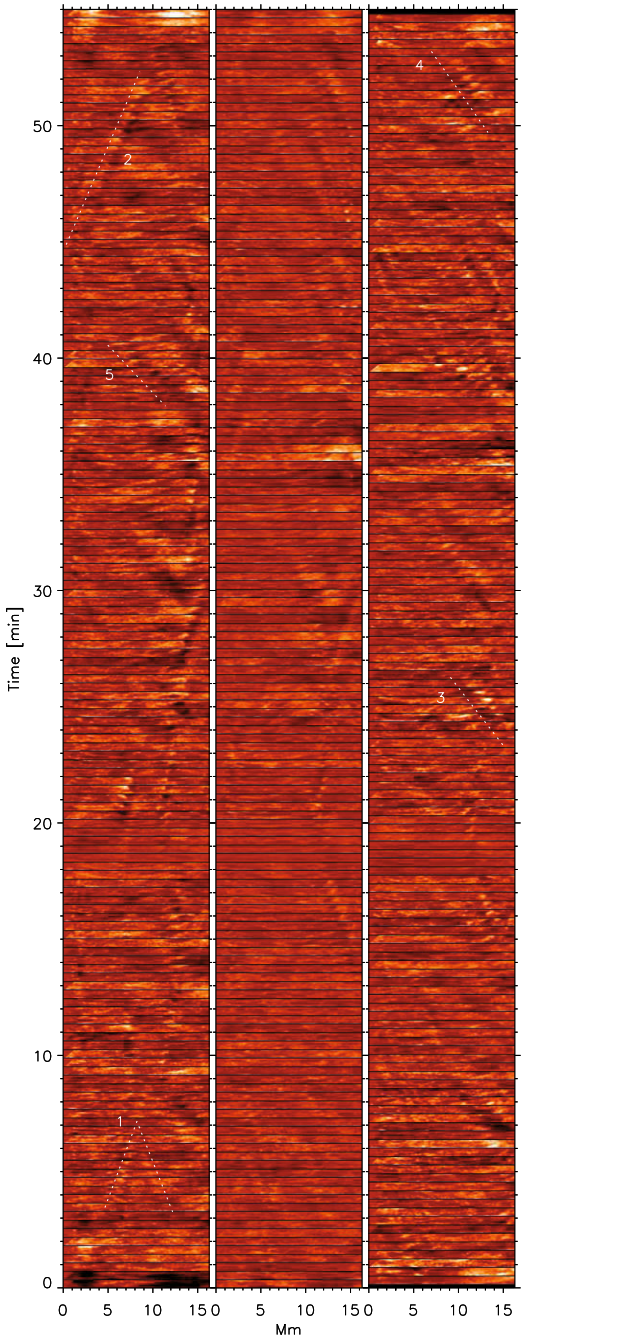

Fig. 8. Example of space-time slices, of 1.″1 width, from AOI D. Same ordering as in Fig. 7.

more pronounced in Doppler-gram and $\Delta I_{0.5}$ slices as at periods 22–40 min in the same figure. The stripes are often bent in the course of the temporal evolution, e.g., the wave parallel to the dashed line "1" in the $\Delta I_{0.5}$ slices of Fig. 7. This wave starts off with a phase velocity of 14 km s^{-1} and speeds up to approximately 40 km s^{-1}, one of the highest velocities measured.

A prominent period is not detected, as already seen in the power spectra of Fig. 6. Sometimes, the waves appear to be repetitive, with two or at most three wave trains in sequence with periods between 90 s and 180 s. An example of consecutive wave trains is indicated by the three dashed lines "2" in the LC slices of Fig. 7. Yet most times, the waves appear as short magnetoacoustic wave trains and packets or pulses traveling across the FOV, like solitary waves. Many of the waves appear to spread out along the direction of propagation and to fade after having traveled a distance of 5–10 Mm.

The amplitudes of the LOS velocities in the Doppler-gram slices are measured to approximately 1 km s^{-1}, be it in the waves with low-phase speeds or in those with high-phase speeds. With the calibration discussed above in the context of the cloud model (see Sect. 2.3), these amplitudes have to be multiplied with a factor of approximately 3. The resulting amplitudes are of the order of 3 km s^{-1}, which is not a small perturbation compared with the

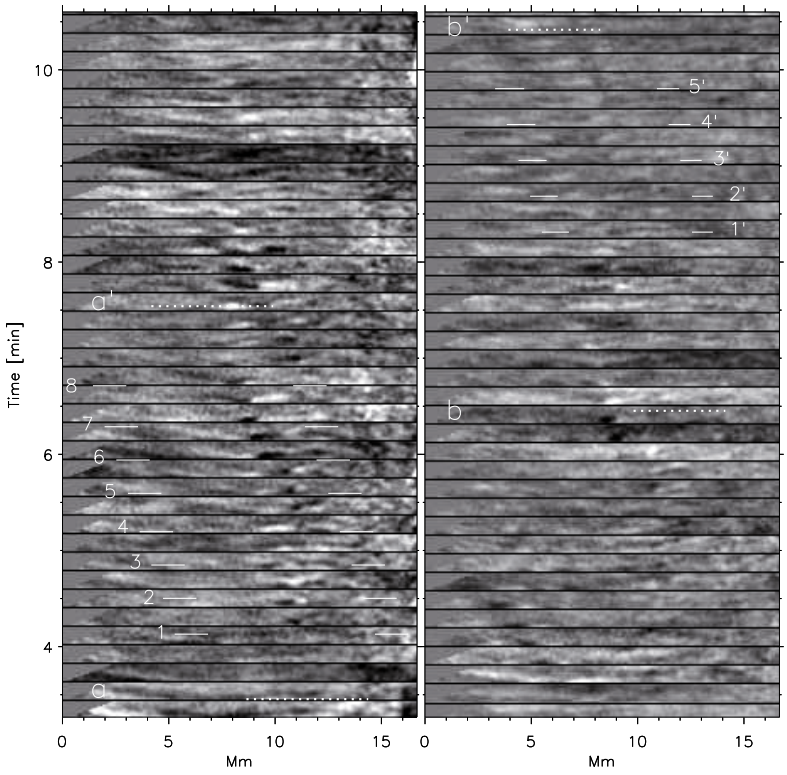

Fig. 9. We show a selected part of space-time slices from AOI C with slice width of 2.″2 showing examples of wave propagation along sinuous channels (*left*, 1−8) and lateral displacements (*right*, chequer-board pattern 1′−5′), see text. *Left column*: Hα line center intensity fluctuations; *right column*: intensity differences at Hα line center: $I_{\rm LC}(t_{i+1})-I_{\rm LC}(t_i)$ with cadence of $\Delta t = t_{i+1}-t_i = 22$ s, referred to as $\Delta I_{\rm LC}$ slices in the text.

sound speed (cf., below the discussion on the magnetoacoustic waves, Sect. 4.2).

Figure 8 from AOI D shows similar space-time slices as those from AOI C in Fig. 7. Also present and more pronounced as in the example shown in Fig. 7, the waves are excited at both sides of the slices and travel into the AOI from both sides, sometimes crossing from the left and the right and possibly colliding as in the example parallel to the dashed lines "1" in the Doppler-gram. The long lasting (more than 7 min), soliton-like wave train (parallel to dashed line "2" in Fig. 8) has a phase velocity of approximately 13 km s^{-1}, a typical speed of the "slow" waves in this AOI. The waves parallel to the dashed lines numbered with "3", "4", and "5" exhibit phase velocities of 26 km s^{-1}, 23 km s^{-1}, and 30 km s^{-1}, respectively, much higher than the sound speed in the chromosphere and in chromospheric structures (cf., below). The amplitudes of the LOS velocities in the waves are again approximately 2−4 km s^{-1} (after the above correction).

We assume that the waves propagate along the dark fibrils and along the magnetic field. There are good reasons to conclude that large parts of the fibrils in AOIs C and D lie parallel to the solar surface. First, the fibrils are rooted at both ends in deeper layers where the excitation of the waves occurs. In between the footpoints, there must be parts parallel to the surface. Second, as mentioned above, the fibrils in AOI D originate with their left parts in the penumbra of a small spot, possibly also those of AOI C, which are thicker on average at their left end than on their right end. They, thus, are similar to superpenumbral Hα fibrils, which form almost horizontal canopies.

The slow waves travel often some 8 Mm with phase velocities of at least 90% of the sound speed (cf. the wave parallel to the dashed line "2" in Fig. 8). It means that the fibrils are inclined with respect to the LOS by at least 65°, which is also suggested by the orientation of the fibrils with respect to the direction of the limb, thus to the LOS in Fig. 2. If the observed gas velocities of 2−4 km s^{-1} represent the LOS component of longitudinal waves, i.e., waves parallel to magnetic fields and fibrils, the *gas* velocities corrected for foreshortening amount to 4.5−9.0 km s^{-1}. This is not small compared to the sound speed. In fact, such high LOS velocities have not been observed either in the waves with propagation close to the direction of LOS at the right end of the slices in Fig. 7. Thus, we suggest that the slow waves are not purely longitudinal waves, but possess a transversal component.

By means of Figs. 9 and 10, we describe two further properties which the waves exhibit occasionally: propagation along sinuous channels and lateral displacements. Figure 9 gives a 7.25 min long section of the temporal development of fluctuations in AOI C with slice widths of 2.″2, but in this case, we show the LC slices and the $\Delta I_{\rm LC}$ slices only. Note that dark and bright features in Hα LC indicate increased and decreased absorption, respectively, *not* enhanced and reduced temperature (see Al et al. 2004; van Noort & Rouppe van der Voort 2006). The two wave packets between the pairs of horizontal dashed lines (a, a′) and (b, b′) have phase speeds of approximately 25 km s^{-1}. Inspection of the LC slices shows that the waves consist of elongated, thin blobs with length of 1″−2″ and width of approximately 0.″5. Apparently, the waves do not travel in the spatial direction along straight lines, but along sinuous lines with deviations from straight lines of <0.″5 in amplitude.

We describe this by means of the waves indicated by the numbers 1−8 in Fig. 9, left panel, and concentrate on the dark blobs and their accompanying brightenings along the direction of propagation. The waves move into the FOV from the right side and propagate along wavy lines, which appear to be fixed for some time, rather than along straight lines. This is shown as an enlargement in Fig. 10 in which Sects. 5 (lower) and 7 (upper panel) are presented again. The dark line in the lower panel indicates the "channel" along which the according wave travels. Such a behaviour suggests that on small scales the magnetic field is not straight and homogeneous, but entangled.

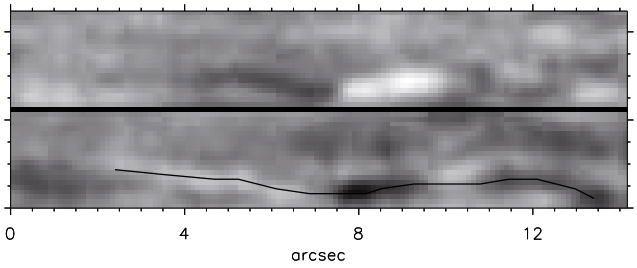

Fig. 10. Parts of the two slices "5" (*lower*) and "7" (*upper*) in Fig. 9. The magnetic channel along which the wave propagates is indicated by the black line in lower slice. Distance of short tickmarks corresponds to 0.″5.

Displacements during the passage of waves are only seen when the waves possess a sufficiently strong component of excursion perpendicular to the LOS. In these cases, the LC slices exhibit a chequer-board pattern since the displacement of absorbing gas produces a displaced darkening and a displaced brightening parallel to it due to reduced absorption. Such a pattern is seen in Fig. 9, left panel, in the wave system between b and b′, especially during the period 8.0−10.5 min. We can modify, or possibly enforce the pattern by taking differences between image slices at subsequent times. This is done with the $\Delta I_{\rm LC}$ slices in the right panel of Fig. 9. At slice indicated by 1′, no intensification of the pattern occurs, but the contrast is enhanced at slice 2′ compared to the pure line center intensity fluctuations. At slices with the numbers 3′ to 5′ the pattern appears reversed.

We summarize in short the observational findings on magnetoacoustic waves:

1. generally, we find two kinds of waves: slow waves with phase velocities of 12−14 km s^{-1} and fast waves with phase velocities of 25−33 km s^{-1} (maximum velocity found 42 km s^{-1}). The waves appear to develop from low-phase speed to high-phase speed waves and vanish after having traveled a distance of 5−10 Mm;
2. irrespective of the wave mode, the LOS gas velocities are of the order of 2−4 km s^{-1};
3. the waves are mainly wave packets or pulses, i.e., solitary waves. They consist of short (1″−2″) and thin (≈0.″5) blobs of compressed gas;
4. the waves appear to follow wiggly, entangled magnetic field lines with possible lateral displacements.

4.2. Interpretation – waves in thin magnetic flux tubes

For the interpretation of the observations from AOI C and D, we adopt the picture of waves in thin magnetic flux tubes, whose radius is small compared to the pressure scale height, as elaborated by Spruit (1982). He assumes a thin, cylindrical magnetic flux tube parallel to the z axis, with radius R, magnetic field along the tube of strength B, pressure p, mass density ρ, and temperature T. The gravity is neglected. The tube is embedded in an external medium with properties $B_{\rm e}$, $p_{\rm e}$, $\rho_{\rm e}$, and $T_{\rm e}$. Inside and outside the tube, the magnetic and atmospheric parameters are constant. In Spruit's (1982) work, the MHD equations are linearized and a mode analysis is performed, with proper conditions at the interface between flux tube and surrounding medium.

Incompressible Alfvén waves ($\nabla\cdot v_1 = 0$, with small velocity perturbation v_1) are also possible in flux tubes. They are torsional Alfvén waves. The compressive solutions lead to

$$\nabla \cdot \boldsymbol{v}_1 = A\,\mathcal{B}_m(nr)\exp[\mathrm{i}\,(\omega t + m\phi + kz)], \tag{4}$$

with amplitude A, $\mathcal{B}_m(nr)$ Bessel functions of order m, r the distance from the axis of the tube, and ϕ the azimuthal angle. Inside the tube, the waves propagate along the z direction. For n the relation holds

$$n^2 = (\omega^2 - v_{\rm A}^2k^2)\,(\omega^2 - c_{\rm s}^2k^2)/[(\omega^2 - c_{\rm t}^2k^2)\,(v_{\rm A}^2 + c_{\rm s}^2)]. \tag{5}$$

Here, the sound velocity and the Alfvén velocity are given by

$$c_{\rm s}^2 = \gamma\frac{p}{\rho} \quad \text{and} \quad v_{\rm A}^2 = \frac{B^2}{4\pi\rho}, \tag{6}$$

respectively, with magnetic field strength B in Gauss, mass density ρ in g cm^{-3}, and gas pressure p in dyn cm^{-2}. B, ρ and p are the unperturbed quantities. In Eq. (5), the tube speed $c_{\rm t}$ is introduced with

$$c_{\rm t}^2 = \frac{v_{\rm A}^2c_{\rm s}^2}{v_{\rm A}^2 + c_{\rm s}^2}, \tag{7}$$

which shows that the tube speed is smaller than both the Alfvén and the sound velocity.

Spruit (1982) showed that in the limit $kR \to 0$ the mode with $m = 0$ is a longitudinal mode with $v_{\rm ph} = c_{\rm t}$, which is approximately the sound speed $c_{\rm s}$ for $v_{\rm A} \gg c_{\rm s}$. This mode is often referred to as the "sausage mode", with velocity inside the tube parallel to the magnetic field.

In the same limit and for $m > 0$, we obtain the so-called "kink waves", with phase speeds related to the magnetic fields and densities through

$$v_{\rm ph}^2 = \frac{\rho v_{\rm A}^2 + \rho_{\rm e}v_{\rm A,e}^2}{\rho + \rho_{\rm e}} = \frac{1}{4\pi}\cdot\frac{B^2 + B_{\rm e}^2}{\rho + \rho_{\rm e}}\,. \tag{8}$$

These waves are transversal waves, and Spruit's (1982) analysis takes into account the dragging by the ambient medium. The phase speeds are obviously $v_{\rm ph}^2 = v_{\rm A}^2$ for $\rho_{\rm e} = \rho$, $B_{\rm e} = B$; $v_{\rm ph}^2 = v_{\rm A}^2/2$ for $\rho_{\rm e} = \rho$, $B_{\rm e} = 0$, and $v_{\rm ph}^2 = 2\cdot v_{\rm A}^2$ for $\rho_{\rm e} = 0$, $B_{\rm e} = B$.

We now compare the observations of waves with the expectation from this linear wave theory. We adopt that the waves propagate along the magnetic field and that the influence of gravity on the wave properties is negligible. The period at the acoustic cutoff of 200 s is longer than the periods, actually seen only rarely, in our data. Likewise, the period for the cutoff of kink waves (Spruit 1981; Choudhuri et al. 1993) is approximately 400 s, for small plasma β, which is the ratio of gas pressure to magnetic pressure, $\beta = (8\pi p)/B^2$.

With the parameters in Table 1 for the surge discussed above in Sect. 3, i.e., with gas pressure $p = 0.38$ dyn cm^{-2} and mass density $\rho = 2.3\times10^{-13}$ g cm^{-3}, the sound velocity is $c_{\rm s} = 16.6$ km s^{-1}. From the determination of parameters in a wide range of chromospheric Hα structures by Tsiropoula & Schmieder (1997), Tsiropoula (2000), and Tsiropoula & Tziotziou (2004) we obtain values of the sound speed in the range of 13.5−16.7 km s^{-1}. The widely-found temperatures of $T = 10^4$ K and the mean molar mass of 0.8 g mol^{-1} from the ionization equilibrium of hydrogen found from Table 1 and from the above works give a sound velocity of 14.4 km s^{-1}. The phase velocities of the slow waves observed here are compatible with

these values, if one accounts for possible small projection effects and for a small reduction for the velocity of tube waves (cf., Eq. (7)).

De Pontieu et al. (2004) adopted magnetic field strengths of the order of 100 Gauss in the chromosphere of active regions. With this value and the commonly found mass densities of $0.8 \ldots 2.3 \times 10^{-13}$ g cm^{-3}, the Alfvén velocity is $v_A = 1000 \ldots 600$ km s^{-1}, much higher than the velocities of the fast waves in the present observations. We believe, that 100 Gauss is an upper limit of the field strengths in the chromosphere of AOIs C and D. From high spatial resolution (approximately 0.″35) data from a plage region by Bello González & Kneer (2008), we find an average field strength in the photosphere of 60–90 Gauss. This may possibly be reduced by a factor of 2 in chromospheric fibrils, as in AOIs C and D, by spreading the field lines over areas which possess little field in the photosphere. Otherwise, the fibrils would not be so elongated. Yet still this yields to Alfvén velocities of $v_A \approx 200$ km s^{-1}, as a minimum value.

Giovanelli (1975) has measured velocities of 70 km s^{-1} in chromospheric Hα structures. With a magnetic field strength of 10 Gauss and with reasonable particle densities, he arrived at an Alfvén velocity in agreement with these measured phase velocities. In the present work, one would need field strengths as low as 5 Gauss for an Alfvén velocity of 32 km s^{-1} as observed. We note that even with 5 Gauss the motions are still dominated by the magnetic field, i.e., $\beta \ll 1$ holds.

We estimate the maximum phase speed measurable from our data to 250–300 km s^{-1}. Such velocities would still be detectable. The phase speeds found here are in the range 25–35 km s^{-1}. The highest measured speed amounts to 42 km s^{-1}. These are obviously incompatible with Alfvén waves in a homogenous magnetic field with 30–100 Gauss. We suggest several possibilities to reconcile our measurements with the picture of fast mode magnetoacoustic waves along the magnetic field, i.e., of Alfvén waves:

1. the magnetic field strength in the fibrils of AOIs C and D is indeed as low as 5 Gauss, which is not very probable considering the very high activity in the whole area observed. The AOIs C and D are not located at the outskirts of this activity;
2. propagation of a fast mode wave in a flux tube surrounded by a medium with low- or zero-field strength, but with high gas density, would reduce the phase speed (cf., Eq. (8));
3. apparently, the waves start as slow mode waves with phase velocities of the order of 10–14 km s^{-1} and then are transformed into fast mode waves propagating with Alfvén velocity. Yet the transformation does not occur immediately. Examples are seen in Fig. 7. While the soliton-like waves evolve into fast mode waves, their wave packets get dispersed, and they decay by spreading out along the direction of propagation;
4. we do not measure phase velocities but group velocities, of solitary wave packets. We have calculated for the slow mode the cusped surface of the wave front according to Ferraro & Plumpton (1966, cf., their Fig. 13), which is rotationally symmetric about the direction of the magnetic field. The adopted Alfvén and sound velocities were 200 km s^{-1} and 16 km s^{-1}, respectively. The maximum velocity of this surface is only marginally larger than the sound speed by 3.2%, and the maximum deviation from the direction of the magnetic field is 0.°01. Thus, the propagation of such slow mode pulses is practically along the magnetic field with the sound velocity;
5. the picture is actually more complicated: the waves with low-phase speed seen here are not pure longitudinal waves. The gas velocities of the waves have a strong transversal component of the order of 3 km s^{-1}. Furthermore, the propagation of the fast waves deviates from straight lines, their motion appears more wiggly, possibly because the magnetic fields are entangled. Under the aspect of these observations the linear theory of small perturbations of straight flux tubes appears to be not sufficient.

5. Conclusions

We have analysed a time sequence of two-dimensional spectrograms in Hα from AR 10875 at $\vartheta \approx 36°$. The observations were taken with the Göttingen Fabry-Perot spectrometer at the Vacuum Tower Telescope at the Observatorio del Teide/Tenerife. The series of 55 min duration, with a cadence or 22 s, shows high spatial resolution of better than 0.″5 in Hα and ∼0.″25 in the accompanying broadband images at 630 nm. Thanks to good resolution, we could follow the evolution of small-scale chromospheric structures on the Sun. From the rich dynamical processes in the observed, very active, flaring region we selected some areas for detailed investigation:

1. A small surge: This surge showed repetitive occurrence with a rate of some 10 min. The surge developed from initial small active fibrils to a straight, thin structure of approximately 15 Mm length, then retreated back to its mouth to reappear again two times. The gas velocities reach approximately 100 km s^{-1}. The rebound shock model by Sterling & Hollweg (1989) seems to be a viable explanation.
2. Two small-scale, synchronous, possibly sympathetic flashes, or mini-flares: In a pair of small areas, two brightenings occurred simultaneously and disappeared during two Hα scans with a total duration of 45 s. Presumably, the evolutionary timescale is much shorter, a few to 10 s. Yet, we could follow the evolution with a temporal resolution of 2 s by analyzing Hα filtergrams at different wavelengths. One of the two flashes showed an apparent proper motion with a speed up to 200 km s^{-1}, while developing a high emission, above the continuum intensity, in the red part of the Hα profile. However, the cadence of the scanning was too slow to decide whether the temporal evolution consisted in a rapid horizontal proper motion with a final fast downflow or in a rapid change of emission at fixed local positions.
3. Magnetoacoustic waves in long fibrils: In two areas with long fibrils, the structures exhibited many magnetoacoustic waves running parallel to the fibrils, thus, presumably also parallel to the magnetic field. The waves travel mostly as short wave trains and packets, i.e., solitary waves. A few times, two or three repetitive wave trains could be seen with periods of 90–180 s. The waves start at the footings of the fibrils with a speed of 12–14 km s^{-1}, which is not much lower than the sound speed estimated for such structures and similar to the tube speed. Most of the waves get accelerated to reach phase speeds of approximately 30 km s^{-1}. Then they spread out along the fibrils and fade. The final phase speed is much lower than the Alfvén speed of ≥200 km s^{-1}, estimated from reasonable magnetic field strengths in the active region chromosphere of 30–100 Gauss and reasonable mass densities in the fibrils of 2×10^{-13} g cm^{-3}. Furthermore, we observe that the slow waves have strong transversal (LOS) velocity components with ∼3 km s^{-1}, i.e., they are not purely longitudinal, and that the fast waves consist of

short (1″−2″), thin (∼0.″5) blobs and apparently move along sinuous lines. We conclude from these findings that a linear theory of wave propagation in straight magnetic flux tubes is not sufficient.

The information contained in the Hα profile in two spatial coordinates and in time sequence turned out to be highly valuable. One can retrieve physical atmospheric parameters in all spatial positions and follow the chromospheric structures during their evolution. Beyond the examples presented above, we could study many more dynamic phenomena in the active solar chromosphere with the present data set.

Yet: "the opportunity makes the thief". We have learned that the sequential scanning with cadence of 22 s is not fast enough in some cases. Temporal resolutions of few seconds, 2−3 s say, are sometimes needed. For future observations, we would design scanning modes of this resolution with images at fewer wavelength positions. Furthermore, future developments of telescopic instrumentation, of adaptive optics, of detectors, and of data analysis including image restoration, will give the required spatial and temporal information about the processes in the solar chromosphere.

Acknowledgements. We thank N. Al Erdoğan for her help with the programs for the lambda-meter method and the analysis with the Hα "cloud model". H. Schleicher is thanked for his kind support with the interpolation of the image sequences to equidistant time steps. B.S.-A.N. acknowledges a stipend-ship from the Max-Planck-Gesellschaft with the International Max Planck Research School on *Physical Processes in the Solar System and Beyond*. N.B.G. and J.B.R. acknowledge financial support by the Deutsche Forschungsgemeinschaft through grants KN 152/31-1 and 418 SPA-112/15/04, respectively. The work of K.G.P. was partially supported by the Deutsche Forschungsgemeinschaft through grant KN 152/29-2. The Vacuum Tower Telescope is operated by the Kiepenheuer-Institut für Sonnenphysik, Freiburg, at the Spanish Observatorio del Teide of the Instituto de Astrofísica de Canarias.

References

Al, N., Bendlin, C., Hirzberger, J., Kneer, F., & Trujillo Bueno, J. 2004, A&A, 418, 1131
Athay, R. G. 1976, The Solar Chromosphere and Corona: Quiet Sun (Dordrecht: Reidel)
Beckers, J. M. 1964, Ph.D. Thesis, Utrecht University
Beckers, J. M., & Tallant, P. E. 1969, Sol. Phys., 7, 351
Bello González, N., & Kneer, F. 2008, A&A, 480, 265
Bello González, N., Okunev, O. V., Domínguez Cerdeña, I., Kneer, F., & Puschmann, K. G. 2005, A&A, 434, 317
Bendlin, C., & Volkmer, R. 1995, A&AS, 112, 371
Bostancı, Z. F. 2005, in Cromospheric and Coronal Magnetic Fields, ed. D. E. Innes, A. Lagg, S. K. Solanki, & D. Danesy, ESA SP-596, on CD ROM, 53.1
Bray, R. J., & Loughhead, R. E. 1974, The Solar Chromosphere (London: Chapman and Hall)
Carlsson, M., & Hansteen, V. 2005, in Chromospheric and Coronal Magnetic Fields, ed. D. Innes, A. Lagg, S. Solanki, & D. Danesy, Proc. Int. Conf., ESA SP-596 (CD ROM), 39
Choudhuri, A. R., Auffret, H., & Priest, E. R. 1993, Sol. Phys., 143, 49
de Boer, C. R. 1996, A&AS, 120, 195
Defouw, R. J. 1976, ApJ, 209, 266
De Moortel, I., Ireland, J., Hood, A. W., & Walsh, R. W. 2002, A&A, 387, L13
De Pontieu, B., Erdélyi, R., & James, S. P. 2004, Nature, 430, 536
Ferraro, V. C. A., & Plumpton, A. 1966, An Introduction to Magneto-Fluid Mechanics (Oxford: Oxford University Press)
Gerogakilas, A. A., Alissandrakis, C. E., & Zachariadis, T. H. 1990, Sol. Phys., 129, 277
Giovanelli, R. 1975, Sol. Phys., 44, 299
Hansteen, V. H., De Pontieu, B., Rouppe van der Voort, L., van Noort, M., & Carlsson, M. 2006, ApJ, 647, L73
Heinzel, P., Dorotovi, I., & Rutten, R. J. 2007, The Physics of Chromospheric Plasmas, ASP Conf. Ser., 368
Hildner, E. 1974, Sol. Phys., 35, 123
Innes, D., Lagg, A., Solanki, S., & Danesy, D. 2005, Chromospheric and Coronal Magnetic Fields, Proc. Intern. Conf., ESA SP-596 (CD ROM)
Keller, C. U., & von der Lühe, O. 1992, A&A, 261, 321
Koschinsky, M., Kneer, F., & Hirzberger, J. 2001, A&A, 365, 588
Krieg, J., Wunnenberg, M., Kneer, F., Koschinsky, M., & Ritter, C. 1999, A&A, 343, 983
Kukhianidze, V., Zakharashvili, T. V., & Khutsishvili, E. 2006, A&A, 449, L35
Musielak, Z. E., Routh, S., & Hammer, R. 2007, ApJ, 659, 650
Priest, E. R. 1984, Solar Magnetohydrodynamics (Dordrecht: Reidel)
Puschmann, K. G., & Sailer, M. 2006, A&A, 454, 1011
Puschmann, K. G., Kneer, F., Seelemann, T., & Wittmann, A. D. 2006, A&A, 445, 337
Robbrecht, E., Verwichte, E., Berghmans, D., et al. 2001, A&A, 370, 591,
Rouppe van der Voort, L. H. M., De Pontieu, B., Hansteen, V. H., Carlsson, M., & van Noort, M. 2007, ApJ, 660, L169
Sánchez-Andrade Nuño, B., Puschmann, K. G., Sánchez Cuberes, M., Blanco Rodríguez, J., & Kneer, F. 2005a, in Chromospheric and Coronal Magnetic Fields, ed. D. Innes, A. Lagg, S. Solanki, & D. Danesy, Proc. Intern. Conf., ESA SP-596 (CD ROM), 62
Sánchez-Andrade Nuño, B., Puschmann, K. G., Sánchez Cuberes, M., Blanco Rodríguez, J., & Kneer, F. 2005b, in The Dynamic Sun: Challenges for Theory and Observations, ed. D. Danesy, S. Poedts, A. De Groof, & J. Andries, Proc. 11th European Solar Physics Meeting, ESA SP-600 (CD ROM), 70
Sánchez-Andrade Nuño, B., Puschmann, K. G., & Kneer, F. 2007, in Modern Solar Facilities – Advanced Solar Science, ed. F. Kneer, K. G. Puschmann, & A. D. Wittmann, Universitätsverlag Göttingen, 273
Spruit, H. C. 1981, A&A, 98, 155
Spruit, H. C. 1982, Sol. Phys., 75, 3
Sterling, A. C., & Hollweg, J. V. 1989, ApJ, 343, 985
Tandberg-Hanssen, E. 1967, Solar Activiy, Blaisdell, Waltham/Mass
Tandberg-Hanssen, E. 1977, in Illustrated Glossary for Solar and Solar-Terrestrial Physics, ed. A. Bruzek, & C. J. Durrant (Dordrecht: Reidel), 97
Tomczyk, S., McIntosh, S. W., Keil, S. L., et al. 2007, Science, 317, 1192
Tothova, D., Innes, D. E., & Solanki, S. K. 2007, in Modern Solar Facilities – Advanced Solar Science, ed. F. Kneer, K. G. Puschmann, & A. D. Wittmann, Universitätsverlag Göttingen, 265
Tripathi, D., Solanki, S. K., Mason, H. E., & Webb, D. F. 2007, A&A, 472, 633
Tsiropoula, G. 2000, A&A, 357, 735
Tsiropoula, G., & Schmieder, B. 1997, A&A, 324, 1183
Tsiropoula, G., & Tziotziou, K. 2004, A&A, 424, 279
Tziotziou, K. 2007, in The Physics of Chromospheric Plasmas, ed. P. Heinzel, I. Dorotovi, & R. J. Rutten, ASP Conf. Ser., 368, 217
Tziotziou, K., Tsiropoula, G., & Mein, P. 2004, A&A, 423, 1133
van Noort, M. J., & Rouppe van der Voort, L. H. M. 2006, ApJ, 648, L67
Volkmer, R., Kneer, F., & Bendlin, C. 1995, A&A, 304, L1
von der Lühe, O. 1984, J. Opt. Soc. Am. A1, 510
von der Lühe, O., Soltau, D., Berkefeld, T., & Schelenz, T. 2003, SPIE, 4853, 187
von Uexküll, M., Kneer, F., & Mattig, W. 1983, A&A, 123, 263
Weigelt, G. P. 1977, Opt. Commun., 21, 55
Wentzel, D. G. 1979, A&A, 76, 20
Wittmann 1969, Sol. Phys., 7, 366
Yi, Z., & Molowny Horas, R. L. 1992, in Proc. from LEST Mini-Workshop, Software for Solar Image Processing, ed. Z. Yi, T. Darvann, & R. Molowny Horas (Oslo: Institute of Theoretical Astrophysics), 69